Microwave Imaging of Buried Objects having Different Permittivities through an Innovative Multi-Frequency Stochastic Method

M. Salucci, L. Poli, N. Anselmi, and A. Massa

Abstract

This work deals with the retrieval of the electromagnetic characteristics of inaccessible subsurface domains by processing ground penetrating radar (*GPR*) data. Assuming a multi-frequency (*MF*) formulation of the buried inverse scattering problem, the solution is obtained by means of a multi-resolution particle swarm optimization (*PSO*) algorithm. The developed *MF-IMSA-PSO* method is able to proficiently exploit the intrinsic frequency diversity of wideband *GPR* measurements in order to mitigate the ill-posedness and non-linearity issues of the subsurface inverse scattering problem. Moreover, thanks to the integration of the *PSO* within the iterative multi-scaling approach (*IMSA*) an increased resolution of the retrieved images is obtained within the identified regions of interest, where the buried objects are supposed to lie. Some numerical experiments are shown in order to assess the effectiveness, the robustness to noise, as well as the current limitations, of the developed method in retrieving buried scatterers having different levels of electric permittivity (i.e., different levels of contrast with respect to the surrounding background medium). Moreover, a direct comparison with respect to the *MF-IMSA-CG*, a state-of-the-art approach based on a conjugate gradient (*CG*) local search algorithm, is given.

1 Definitions

1.1 Glossary

- SF: Single-Frequency;
- FH: Frequency-Hopping;
- MF: Multi-Frequency;
- P: Swarm dimension;
- U: Total number of unknowns;
- S: Maximum number of $IMSA$ zooming steps;
- s^{best}: Last performed $IMSA$ zooming step ($s^{best} \leq S$);
- η_{th}: $IMSA$ zooming threshold;
- D_{inv}: Investigation domain;
- D_{obs}: Observation domain;
- L: Side of the investigation domain;
- N: Number of discretization cells in D_{ind};
- V: Number of views;
- M: Number of measurement points;
- F: Number of frequencies considered for the inversion;
- $\mathbf{r}^{(v)} = \left(x^{(v)}, y^{(v)}\right)$: Coordinates of the v-th source ($v = 1, \ldots, V$).
- $\mathbf{r}_m^{(v)} = \left(x_m^{(v)}, y_m^{(v)}\right)$: Coordinates of the m-th measurement point for the v-th view v, ($m = 1, \ldots, M$);
- $\varepsilon_{ra} = \frac{\varepsilon_a}{\varepsilon_0}$: Relative electric permittivity for the upper half-space ($y > 0$);
- σ_a: Conductivity for the upper half-space ($y > 0$);
- $\varepsilon_{rb} = \frac{\varepsilon_b}{\varepsilon_0}$: Background relative electric permittivity;
- σ_b: Background conductivity;
- $E_{inc}^{(v)}(\mathbf{r}_n; f)$: Measured internal incident field inside the n-th cell, for the v-th view at frequency f;
- $\widetilde{E}_{inc}^{(v)}(\mathbf{r}_n; f)$: Computed internal incident field inside the n-th cell, for the v-th view at frequency f;
- $E_{scatt}^{(v)}\left(\mathbf{r}_m^{(v)}; f\right)$: Measured external scattered by the m-th measurement point, for the v-th view at frequency f;
- $\widetilde{E}_{scatt}^{(v)}\left(\mathbf{r}_m^{(v)}; f\right)$: Measured external scattered by the m-th measurement point, for the v-th view at frequency f.

1.2 Contrast function

The contrast function at frequency f is defined as

$$\tau(\mathbf{r}; f) = \frac{\varepsilon_{eq}(\mathbf{r}) - \varepsilon_{eqb}}{\varepsilon_0} = [\varepsilon_r(\mathbf{r}) - \varepsilon_{rb}] + j\left[\frac{\sigma_b - \sigma(\mathbf{r})}{2\pi f \varepsilon_0}\right]$$

where

- $\mathbf{r} = (x, y)$: position vector;
- $\Re\{\tau(\mathbf{r}; f)\} = [\varepsilon_r(\mathbf{r}) - \varepsilon_{rb}]$;
- $\Im\{\tau(\mathbf{r}; f)\} = \left[\frac{\sigma_b - \sigma(\mathbf{r})}{2\pi f \varepsilon_0}\right]$;
- $\varepsilon_{eq}(\mathbf{r}) = \varepsilon_0 \varepsilon_r(\mathbf{r}) - j\frac{\sigma(\mathbf{r})}{2\pi f}$;
- $\varepsilon_{eqb} = \varepsilon_0 \varepsilon_{rb} - j\frac{\sigma_b}{2\pi f}$;
- $\varepsilon_r(\mathbf{r})$: relative electric permittivity at position $\mathbf{r}$;
- $\sigma(\mathbf{r})$: conductivity at position $\mathbf{r}$;

NOTE: we assume that $\varepsilon_r(\mathbf{r})$ and $\sigma(\mathbf{r})$ are **not frequency dependent** (non-dispersive mediums).

1.2.1 Contrast function and reference frequency f_{ref} (MF approaches)

The contrast function at a generic frequency f can be expressed by means of the contrast function computed for a selected reference frequency

$$f = f_{ref} \tag{1}$$

as follows

$$\tau(\mathbf{r}; f) = \Re\{\tau(\mathbf{r}; f_{ref})\} + j\frac{f_{ref}}{f}\Im\{\tau(\mathbf{r}; f_{ref})\}. \tag{2}$$

This allows to reduce the number of unknowns when dealing with multi-frequency techniques, since we can just consider the contrast function at the reference frequency.

1.3 Cost function & unknowns

1.3.1 Multi-Frequency (MF) approaches

These approaches jointly consider data at F frequencies. The functional minimized by the inversion algorithm is defined as

$$\Phi(\mathbf{x}) = \Phi_{state}(\mathbf{x}) + \Phi_{data}(\mathbf{x}) \tag{3}$$

where $\Phi_{state}(\mathbf{x})$ and $\Phi_{data}(\mathbf{x})$ are respectively the data and state terms of the cost function, defined as

$$\Phi_{state}(\mathbf{x}) = \frac{\sum_{j=1}^{F}\sum_{v=1}^{V}\sum_{n=1}^{N}\left|E_{inc}^{(v)}(\mathbf{r}_n; f_j) - \widetilde{E}_{inc}^{(v)}(\mathbf{r}_n; f_j)\right|^2}{\sum_{j=1}^{F}\sum_{v=1}^{V}\sum_{n=1}^{N}\left|E_{inc}^{(v)}(\mathbf{r}_n; f_j)\right|^2} \tag{4}$$

$$\Phi_{data} = \frac{\sum_{j=1}^{F}\sum_{v=1}^{V}\sum_{m=1}^{M}\left|E_{scatt}^{(v)}\left(\mathbf{r}_m^{(v)}; f_j\right) - \widetilde{E}_{scatt}^{(v)}\left(\mathbf{r}_m^{(v)}; f_j\right)\right|^2}{\sum_{j=1}^{F}\sum_{v=1}^{V}\sum_{m=1}^{M}\left|E_{scatt}^{(v)}\left(\mathbf{r}_m^{(v)}; f_j\right)\right|^2} \tag{5}$$

The unknowns of the inversion problem are

$$\mathbf{x} = \left\{\tau(\mathbf{r}; f_{ref}); E_{tot}^{(v)}(\mathbf{r}_n; f_j)\right\} \qquad n = 1, ..., N; v = 1, ..., V; j = 1, ..., F. \tag{6}$$

The total number of unknowns for MF-based approaches is then given by

$$U_{MF} = 2N(1 + VF). \tag{7}$$

1.4 Reconstruction errors

The following integral error is defined

$$\Xi_{reg} = \frac{1}{N_{reg}}\sum_{n=1}^{N_{reg}}\frac{|\tau_n^{act} - \tau_n^{rec}|}{|\tau_n^{act} + 1|} \tag{8}$$

where reg indicates if the error computation covers

- the overall investigation domain ($reg \Rightarrow tot$),
- the actual scatterer support ($reg \Rightarrow int$),
- or the background region ($reg \Rightarrow ext$).

2 Numerical Results: Variation of the Object Relative Permittivity

2.1 Circular empty object ($\sigma_{obj} = 10^{-3}$ [S/m])

2.1.1 Parameters

Background

Inhomogeneous and nonmagnetic background composed by two half spaces

- Upper half space ($y > 0$ - air): $\varepsilon_{ra} = 1.0$, $\sigma_a = 0.0$;
- Lower half space ($y < 0$ - soil): $\varepsilon_{rb} = 4.0$, $\sigma_b = 10^{-3}$[S/m];

Investigation domain (D_{inv})

- Side: $L_{D_{inv}} = 0.8$ [m];
- Barycenter: $\left(x_{bar}^{D_{inv}}, y_{bar}^{D_{inv}}\right) = (0.00, -0.4)$ [m];

Time-Domain forward solver ($FDTD$ - $GPRMax2D$)

- Side of the simulated domain: $L = 6$ [m];
- Number of cells: $N^{FDTD} = 750 \times 750 = 5.625 \times 10^5$;
- Side of the $FDTD$ cells $l^{FDTD} = 0.008$ [m];
- Simulation time window: $T^{FDTD} = 20 \times 10^{-9}$ [sec];
- Time step: $\Delta t^{FDTD} = 1.89 \times 10^{-11}$ [sec];
- Number of time samples: $N_t^{FDTD} = 1060$;
- Boundary conditions: perfectly matched layer (PML);
- Source type: Gaussian mono-cycle (first Gaussian pulse derivative, called "Ricker" in $GPRMax2D$)
  - Central frequency: $f_0 = 300$ [MHz];
  - Source amplitude: $A = 1.0$ [A];

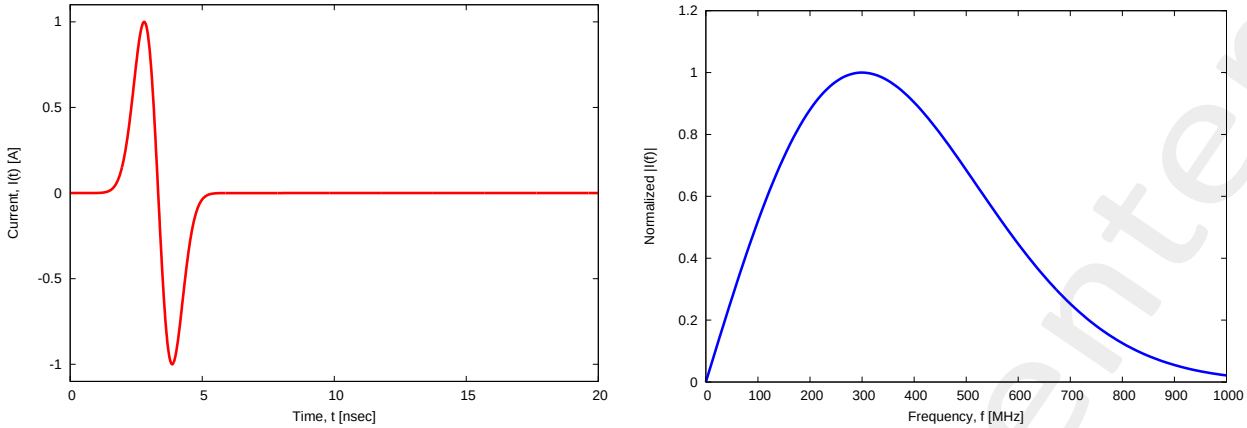

(a) (b)

Figure 1: $GPRMax2D$ excitation signal. (a) Time pulse, (b) normalized frequency spectrum.

Frequency parameters

- Frequency range: $f \in [f_{min}, f_{max}] = [200.0, 600.0]$ [MHz] (-3 [dB] bandwidth of the Gaussian Monocycle excitation centered at $f_0 = 300$ [MHz]);
- Frequency step: $\Delta f = 100$ [MHz] ($F = 5$ frequency steps in $[f_{min}, f_{max}]$);

f [MHz]	λ_a [m]	λ_b [m]	f^* [MHz]
200.0	1.50	0.75	200.5
300.0	1.00	0.50	297.6
400.0	0.75	0.37	401.1
500.0	0.60	0.30	498.1
600.0	0.50	0.25	601.6

Table 1: Considered frequencies and corresponding wavelength in the upper medium (λ_a, free space) and in the lower medium (λ_b, soil). f^* is the nearest frequency sample available from transformed time-domain data, and represents the real frequency considered by the inversion algorithm.

Scatterer

- Type: Circular;
- Barycenter: $(x_{obj}, y_{obj}) = (0.0, -0.4)$ [m];
- Radius: $r_{obj}^{int} = 0.08$ [m], $r_{obj}^{ext} = 0.12$ [m];
- Electromagnetic properties: $\varepsilon_{r,obj} = \{4.5; 5.0; 5.5; 6.0; 6.5; 7.0\}$, $\sigma_{obj} = 10^{-3}$ [S/m] ($\sigma_{obj} = \sigma_b$);
- Contrast function: $\tau = \{0.5; 1.0; 1.5; 2.0; 2.5; 3.0\}$

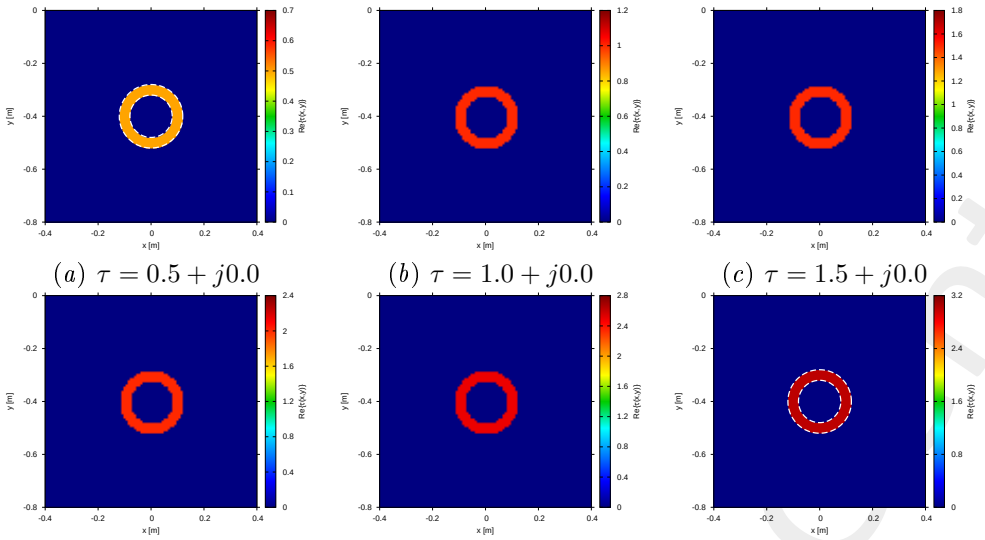

$(a)\ \tau = 0.5 + j0.0$ $(b)\ \tau = 1.0 + j0.0$ $(c)\ \tau = 1.5 + j0.0$

$(d)\ \tau = 2.0 + j0.0$ $(e)\ \tau = 2.5 + j0.0$ $(f)\ \tau = 3.0 + j0.0$

Figure 2: Actual object.

Measurement setup

- Considered frequency: $f_{min} = 200$ [MHz], $\lambda_b = 0.75$ [m]. [1]
- $\#DoFs = 2ka = \frac{2\pi}{\lambda_b} L\sqrt{2} = \frac{2\pi}{0.75} 0.8\sqrt{2} \simeq 9.5$;
- Number of views (sources): $V = 10$;
  - $\min\{x_v\} = -0.5$ [m], $\max\{x_v\} = 0.5$ [m];
  - height: $y_v = 0.1$ [m], $\forall v = 1, \ldots, V$;
- Number of measurement points: $M = 9$;
  - $\min\{x_m\} = -0.5$ [m], $\max\{x_m\} = 0.5$ [m];
  - height: $y_m = 0.1$ [m], $\forall m = 1, \ldots, M$;

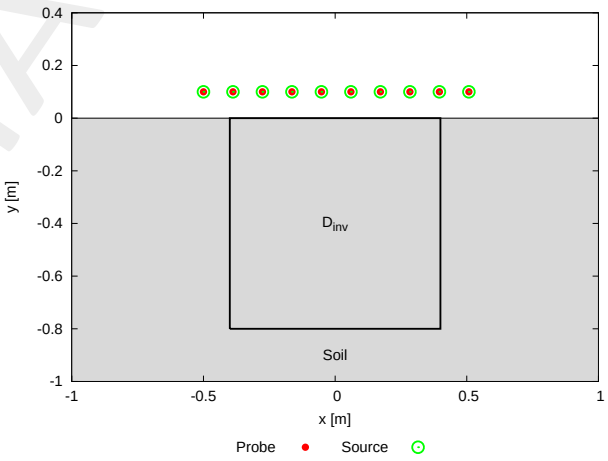

Figure 3: Location of the measurement points ($M = 9$) and of the sources ($V = 10$). Only one source is active for each view.

[1] **NOTE:** This choice is done in order to keep the number of unknowns lower than 5000.

Inverse solver parameters

- **Shared parameters**
  - Number of unknowns: $U = 2N\left(1 + VF\right) = 4998$;
  - Weight of the state term of the functional: 1.0;
  - Weight of the data term of the functional: 1.0;
  - Weight of the penalty term of the functional: 0.0;
  - Convergence threshold: 10^{-10};
  - Variable ranges:
    - $\sigma \in \left[8.0 \times 10^{-4}, 1.2 \times 10^{-3}\right]$ [S/m];
    - $\Re\left\{E_{tot}^{int}\right\} \in [-8, 8]$, $\Im\left\{E_{tot}^{int}\right\} \in [-8, 8]$;
  - Degrees of freedom:
    - Considered frequency: $f_{min} = 200$ [MHz], $\lambda_b = 0.75$ [m];
    - $\frac{(2ka)^2}{2} = \frac{\left(2 \times \frac{2\pi}{\lambda_b} \times \frac{L\sqrt{2}}{2}\right)^2}{2} = 4\pi^2 \left(\frac{L}{\lambda_b}\right)^2 = 4\pi^2 \left(\frac{0.8}{0.75}\right)^2 \simeq 44.87$;
  - Number of cells: $N = 49 = 7 \times 7$;
  - Maximum number of $IMSA$ steps: $S = 4$;
  - Side ratio threshold: $\eta_{th} = 0.2$;
- $MF - IMSA - PSO$ **parameters**
  - Maximum number of iterations: $I = 20000$;
  - Swarm dimension: $P = \frac{5}{100} \times U = 250$;
  - $C_1 = C_2 = 2.0$;
  - Inertial weight: $w = 0.4$;
  - Velocity clamping: enabled;
- $MF - IMSA - CG$ **parameters**
  - Maximum number of iterations: $I = 200$;

Signal to noise ratio (on $E_{tot}\left(t\right)$)

- $SNR = \{50, 40, 30, 20\}$ [dB] + Noiseless data.

2.1.2 $\varepsilon_{r,obj} = 4.5$ $(\tau = 0.5)$ - $MF-IMSA-PSO$ vs. $MF-IMSA-CG$: Final reconstructions

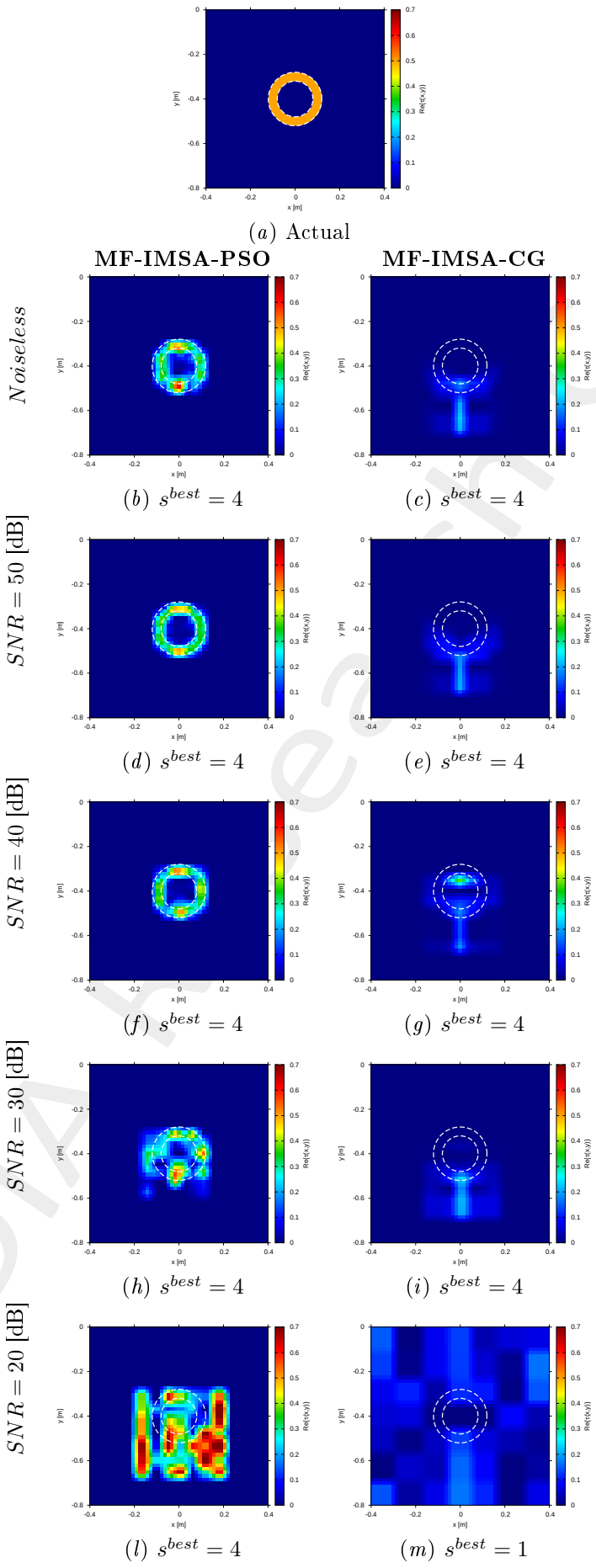

(a) Actual

(b) $s^{best} = 4$ (c) $s^{best} = 4$

(d) $s^{best} = 4$ (e) $s^{best} = 4$

(f) $s^{best} = 4$ (g) $s^{best} = 4$

(h) $s^{best} = 4$ (i) $s^{best} = 4$

(l) $s^{best} = 4$ (m) $s^{best} = 1$

Figure 4: $MF-IMSA-PSO$ vs. $MF-IMSA-CG$: Retrieved dielectric profiles at the $IMSA$ convergence step (s^{best}).

2.1.3 $\varepsilon_{r,obj} = 5.0$ ($\tau = 1.0$) - $MF-IMSA-PSO$ vs. $MF-IMSA-CG$: Final reconstructions

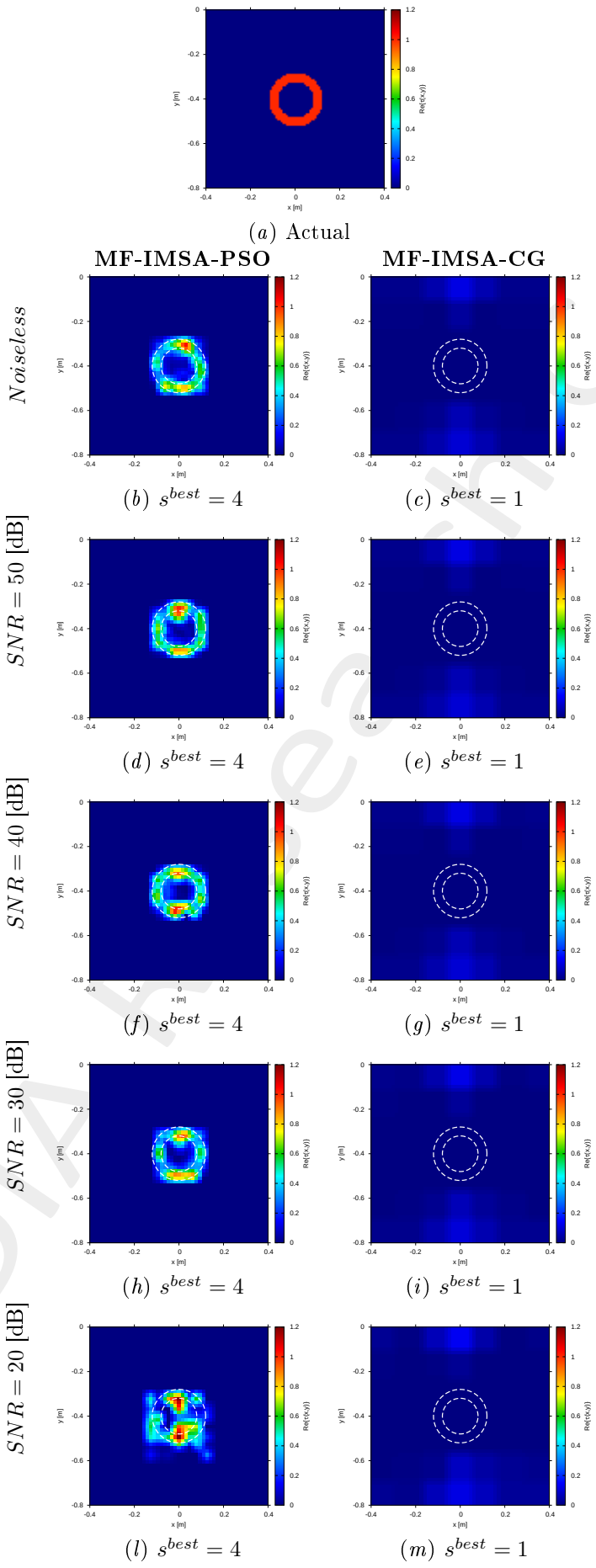

Figure 5: $MF-IMSA-PSO$ vs. $MF-IMSA-CG$: Retrieved dielectric profiles at the $IMSA$ convergence step (s^{best}).

2.1.4 $\varepsilon_{r,obj} = 5.5$ ($\tau = 1.5$) - $MF-IMSA-PSO$ vs. $MF-IMSA-CG$: Final reconstructions

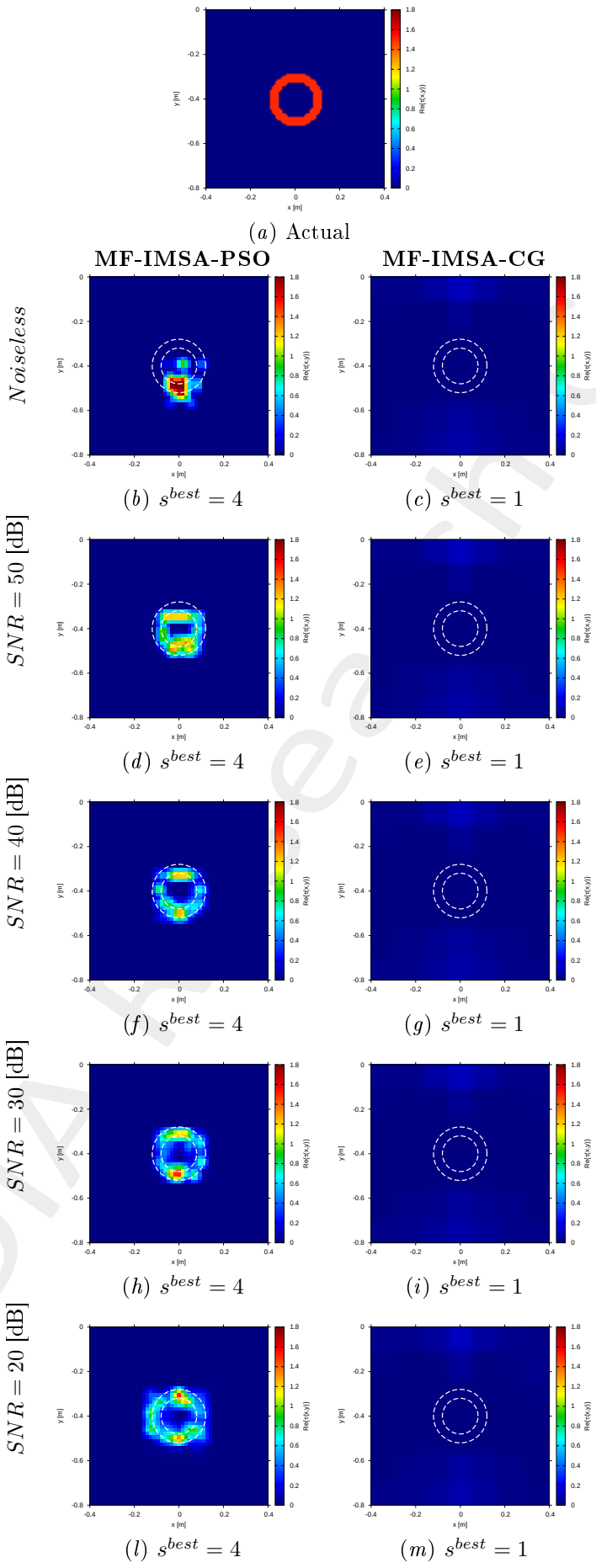

Figure 6: $MF-IMSA-PSO$ vs. $MF-IMSA-CG$: Retrieved dielectric profiles at the $IMSA$ convergence step (s^{best}).

2.1.5 $\varepsilon_{r,obj} = 6.0$ ($\tau = 2.0$) - $MF-IMSA-PSO$ vs. $MF-IMSA-CG$: Final reconstructions

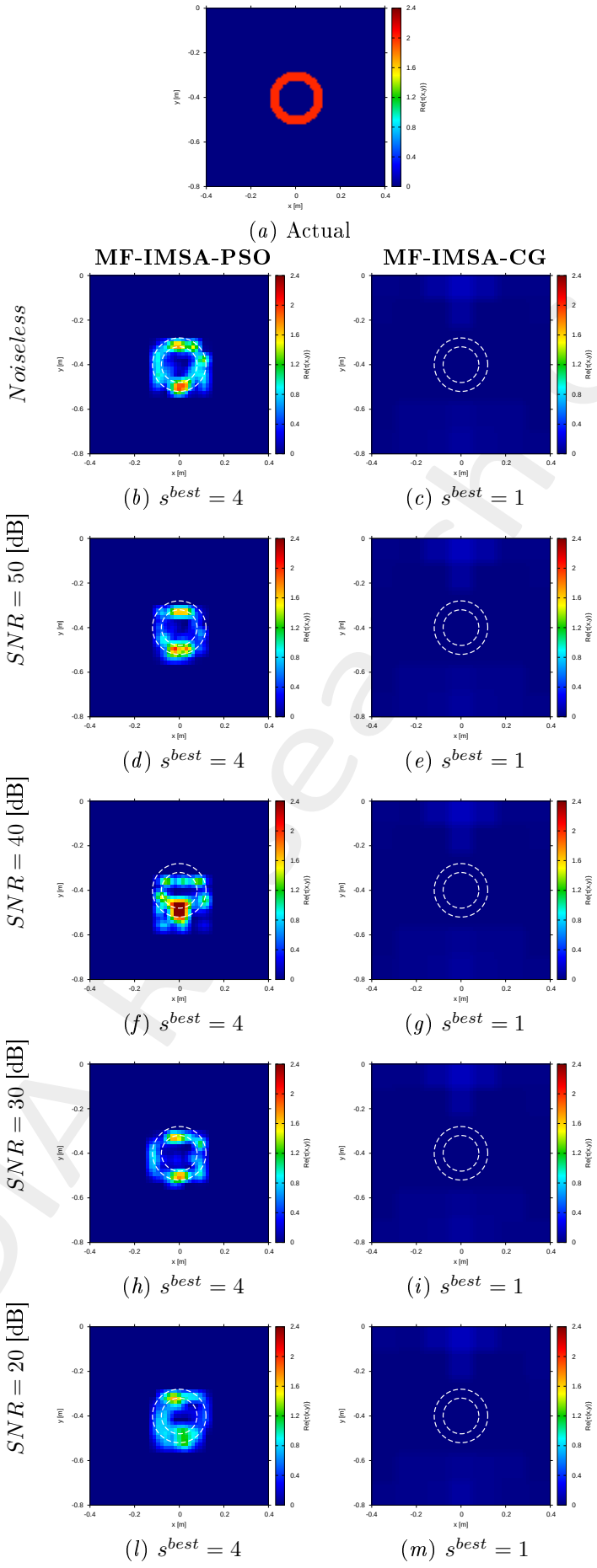

Figure 7: $MF-IMSA-PSO$ vs. $MF-IMSA-CG$: Retrieved dielectric profiles at the $IMSA$ convergence step (s^{best}).

2.1.6 $\varepsilon_{r,obj} = 6.5$ ($\tau = 2.5$) - $MF-IMSA-PSO$ vs. $MF-IMSA-CG$: Final reconstructions

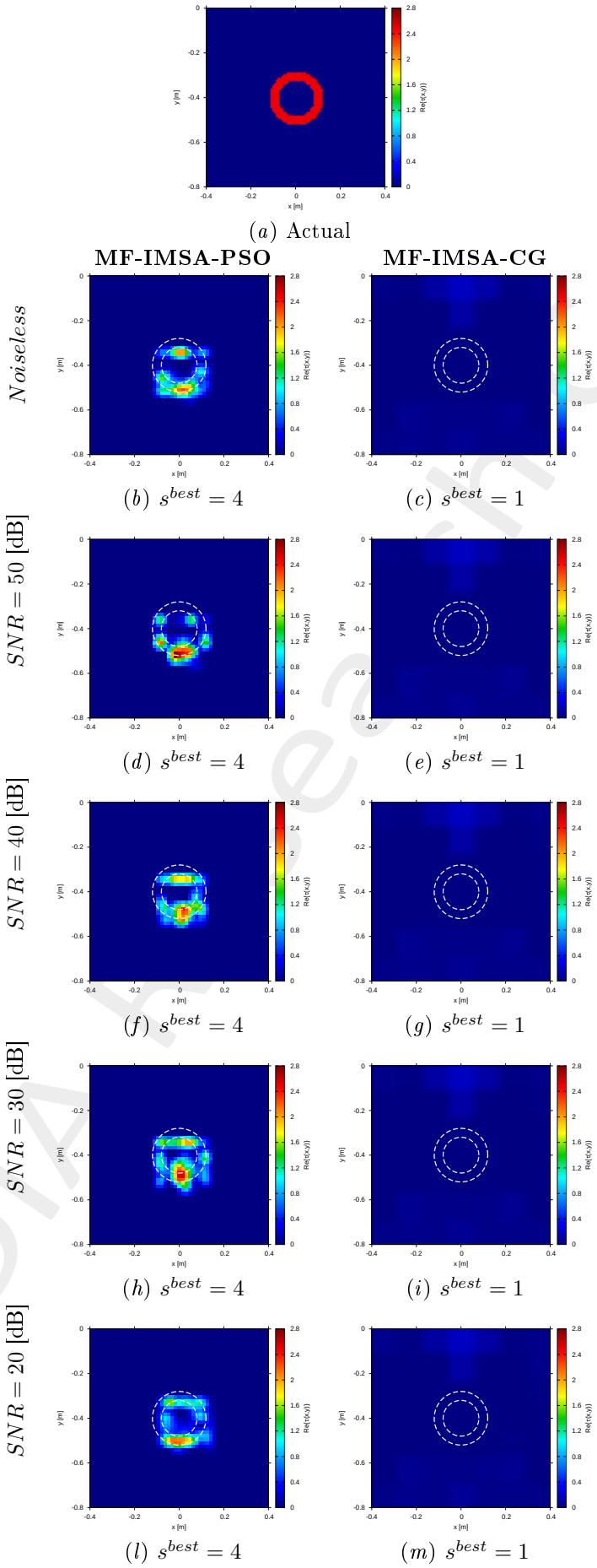

Figure 8: $MF-IMSA-PSO$ vs. $MF-IMSA-CG$: Retrieved dielectric profiles at the $IMSA$ convergence step (s^{best}).

2.1.7 $\varepsilon_{r,obj} = 7.0$ ($\tau = 3.0$) - $MF-IMSA-PSO$ vs. $MF-IMSA-CG$: Final reconstructions

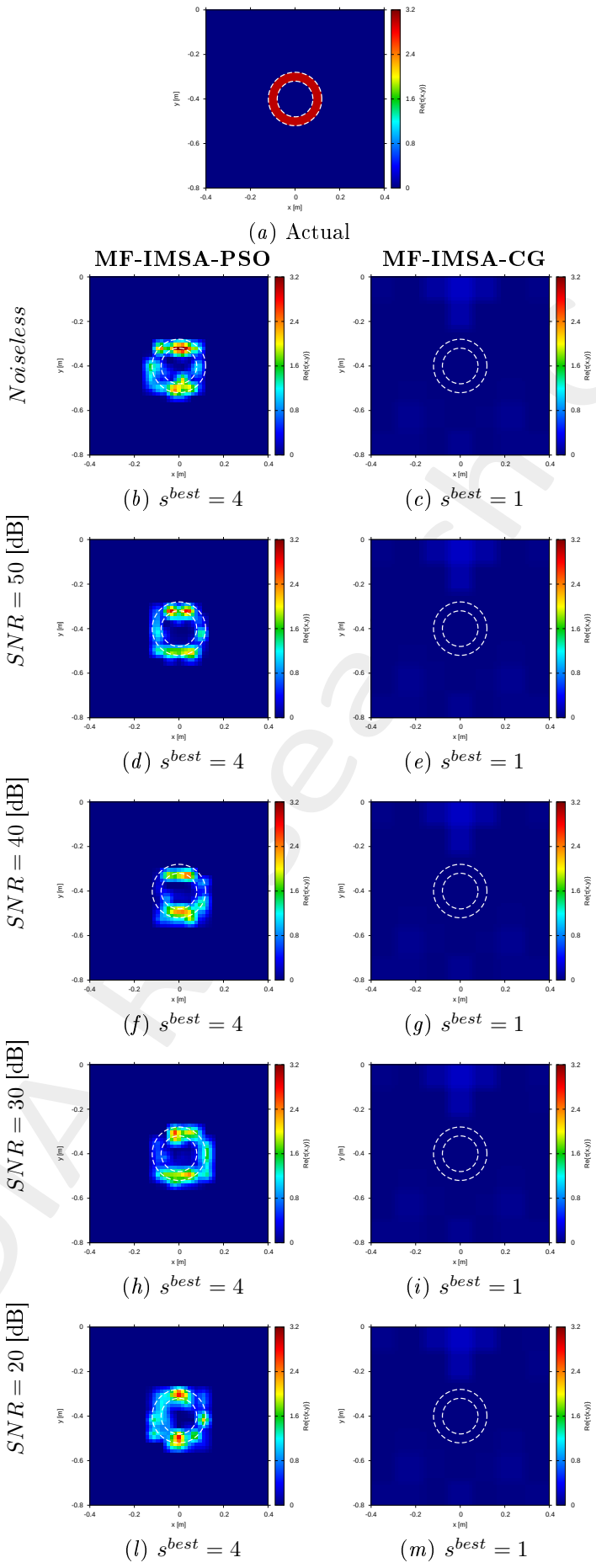

Figure 9: $MF-IMSA-PSO$ vs. $MF-IMSA-CG$: Retrieved dielectric profiles at the $IMSA$ convergence step (s^{best}).

2.1.8 $MF-IMSA-PSO$ vs. $MF-IMSA-CG$: Errors vs. $\varepsilon_{r,obj}$

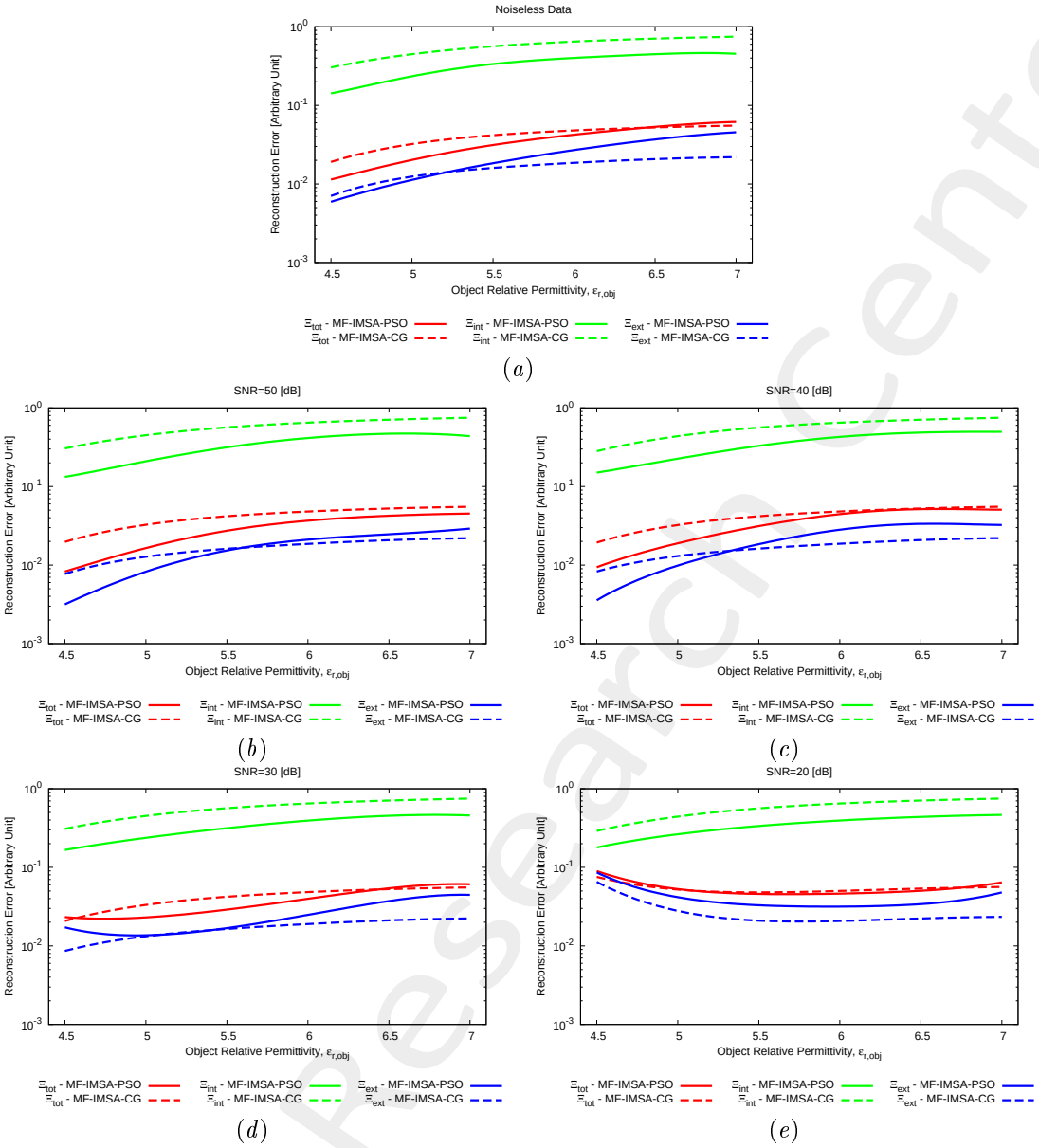

Figure 10: $MF-IMSA-PSO$ vs. $MF-IMSA-CG$: Reconstruction errors vs. the object relative permittivity ($\varepsilon_{r,obj}$).

2.1.9 $MF-IMSA-PSO$ vs. $MF-IMSA-CG$: Errors vs. SNR

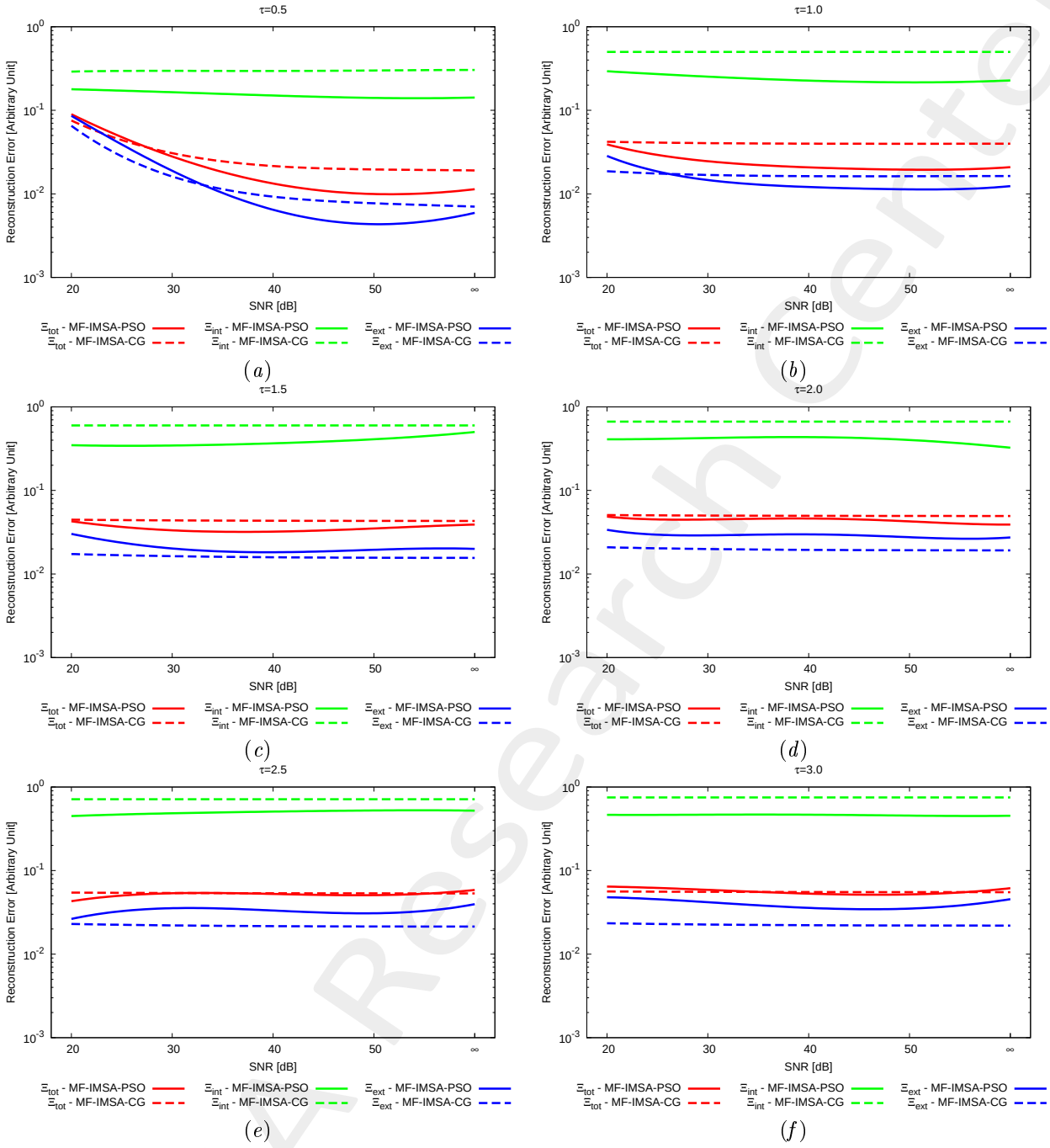

Figure 11: $MF-IMSA-PSO$ vs. $MF-IMSA-CG$: Reconstruction errors vs. SNR.

2.2 $\mathcal{I}$-Shaped object ($\sigma_{obj} = 10^{-3}$ [S/m])

2.2.1 Parameters

Background

Inhomogeneous and nonmagnetic background composed by two half spaces

- Upper half space ($y > 0$ - air): $\varepsilon_{ra} = 1.0$, $\sigma_a = 0.0$;
- Lower half space ($y < 0$ - soil): $\varepsilon_{rb} = 4.0$, $\sigma_b = 10^{-3}$[S/m];

Investigation domain (D_{inv})

- Side: $L_{D_{inv}} = 0.8$ [m];
- Barycenter: $\left(x_{bar}^{D_{inv}}, y_{bar}^{D_{inv}}\right) = (0.00, -0.4)$ [m];

Time-Domain forward solver ($FDTD$ - $GPRMax2D$)

- Side of the simulated domain: $L = 6$ [m];
- Number of cells: $N^{FDTD} = 750 \times 750 = 5.625 \times 10^5$;
- Side of the $FDTD$ cells $l^{FDTD} = 0.008$ [m];
- Simulation time window: $T^{FDTD} = 20 \times 10^{-9}$ [sec];
- Time step: $\Delta t^{FDTD} = 1.89 \times 10^{-11}$ [sec];
- Number of time samples: $N_t^{FDTD} = 1060$;
- Boundary conditions: perfectly matched layer (PML);
- Source type: Gaussian mono-cycle (first Gaussian pulse derivative, called "Ricker" in $GPRMax2D$)
  - Central frequency: $f_0 = 300$ [MHz];
  - Source amplitude: $A = 1.0$ [A];

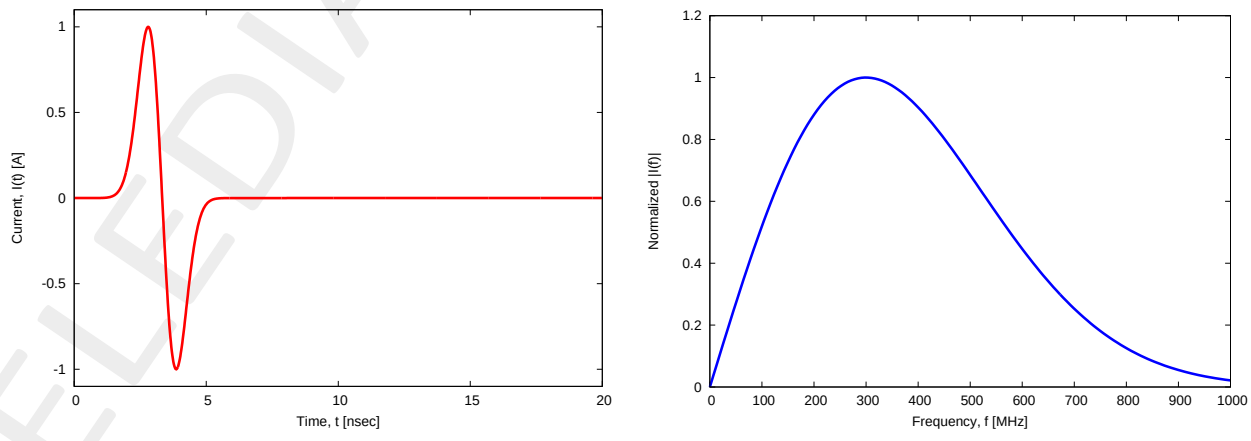

(a) (b)

Figure 12: $GPRMax2D$ excitation signal. (a) Time pulse, (b) normalized frequency spectrum.

Frequency parameters

- Frequency range: $f \in [f_{min}, f_{max}] = [200.0, 600.0]$ [MHz] (-3 [dB] bandwidth of the Gaussian Monocycle excitation centered at $f_0 = 300$ [MHz]);
- Frequency step: $\Delta f = 100$ [MHz] ($F = 5$ frequency steps in $[f_{min}, f_{max}]$);

f [MHz]	λ_a [m]	λ_b [m]	f^* [MHz]
200.0	1.50	0.75	200.5
300.0	1.00	0.50	297.6
400.0	0.75	0.37	401.1
500.0	0.60	0.30	498.1
600.0	0.50	0.25	601.6

Table 2: Considered frequencies and corresponding wavelength in the upper medium (λ_a, free space) and in the lower medium (λ_b, soil). f^* is the nearest frequency sample available from transformed time-domain data, and represents the real frequency considered by the inversion algorithm.

Scatterer

- Type: $\mathcal{I}$-Shaped;
- Electromagnetic properties: $\varepsilon_{r,obj} = \{4.5; 5.0; 5.5; 6.0; 6.5; 7.0\}$, $\sigma_{obj} = 10^{-3}$ [S/m] ($\sigma_{obj} = \sigma_b$);
- Contrast function: $\tau = \{0.5; 1.0; 1.5; 2.0; 2.5; 3.0\}$

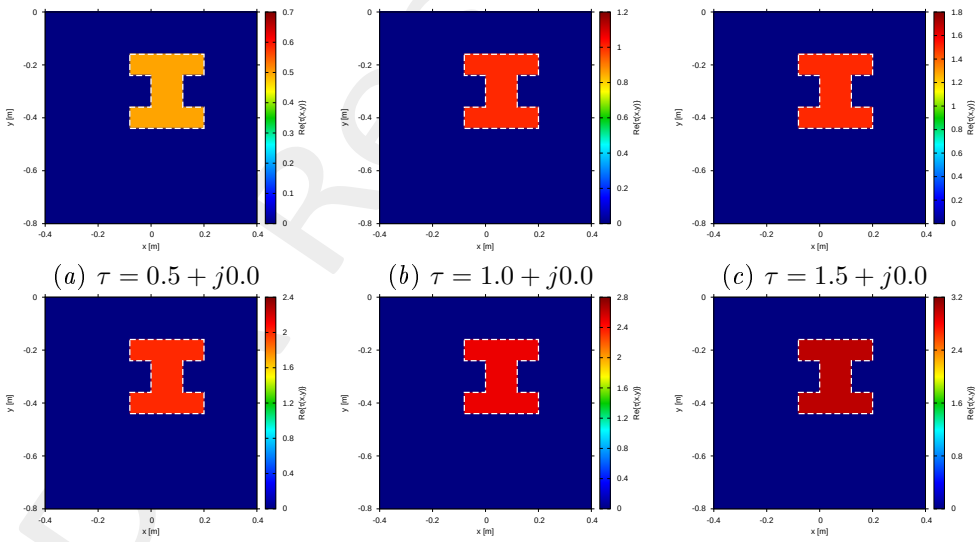

(a) $\tau = 0.5 + j0.0$ (b) $\tau = 1.0 + j0.0$ (c) $\tau = 1.5 + j0.0$

(d) $\tau = 2.0 + j0.0$ (e) $\tau = 2.5 + j0.0$ (f) $\tau = 3.0 + j0.0$

Figure 13: Actual object.

Measurement setup

- Considered frequency: $f_{min} = 200$ [MHz], $\lambda_b = 0.75$ [m]. [2]
- $\#DoFs = 2ka = \frac{2\pi}{\lambda_b} L\sqrt{2} = \frac{2\pi}{0.75} 0.8\sqrt{2} \simeq 9.5$;

[2] **NOTE:** This choice is done in order to keep the number of unknowns lower than 5000.

- Number of views (sources): $V = 10$;
  - $\min\{x_v\} = -0.5$ [m], $\max\{x_v\} = 0.5$ [m];
  - height: $y_v = 0.1$ [m], $\forall v = 1, \ldots, V$;
- Number of measurement points: $M = 9$;
  - $\min\{x_m\} = -0.5$ [m], $\max\{x_m\} = 0.5$ [m];
  - height: $y_m = 0.1$ [m], $\forall m = 1, \ldots, M$;

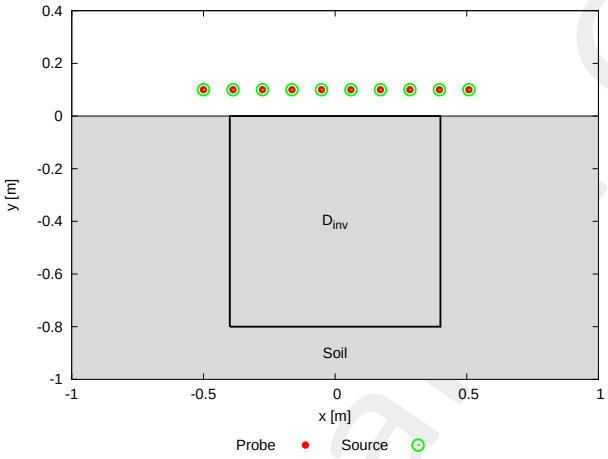

Figure 14: Location of the measurement points ($M = 9$) and of the sources ($V = 10$). Only one source is active for each view.

Inverse solver parameters

- **Shared parameters**
  - Number of unknowns: $U = 2N\,(1 + VF) = 4998$;
  - Weight of the state term of the functional: 1.0;
  - Weight of the data term of the functional: 1.0;
  - Weight of the penalty term of the functional: 0.0;
  - Convergence threshold: 10^{-10};
  - Variable ranges:
    - $\sigma \in \left[8.0 \times 10^{-4}, 1.2 \times 10^{-3}\right]$ [S/m];
    - $\Re\left\{E_{tot}^{int}\right\} \in [-8, 8]$, $\Im\left\{E_{tot}^{int}\right\} \in [-8, 8]$;
  - Degrees of freedom:
    - Considered frequency: $f_{min} = 200$ [MHz], $\lambda_b = 0.75$ [m];
    - $\frac{(2ka)^2}{2} = \frac{\left(2 \times \frac{2\pi}{\lambda_b} \times \frac{L\sqrt{2}}{2}\right)^2}{2} = 4\pi^2 \left(\frac{L}{\lambda_b}\right)^2 = 4\pi^2 \left(\frac{0.8}{0.75}\right)^2 \simeq 44.87$;
  - Number of cells: $N = 49 = 7 \times 7$;

  - Maximum number of $IMSA$ steps: $S = 4$;
  - Side ratio threshold: $\eta_{th} = 0.2$;

- $MF - IMSA - PSO$ **parameters**
  - Maximum number of iterations: $I = 20000$;
  - Swarm dimension: $P = \frac{5}{100} \times U = 250$;
  - $C_1 = C_2 = 2.0$;
  - Inertial weight: $w = 0.4$;
  - Velocity clamping: enabled;

- $MF - IMSA - CG$ **parameters**
  - Maximum number of iterations: $I = 200$;

Signal to noise ratio (on $E_{tot}(t)$)

- $SNR = \{50, 40, 30, 20\}$ [dB] + Noiseless data.

2.2.2 $\varepsilon_{r,obj} = 4.5$ $(\tau = 0.5)$ - $MF-IMSA-PSO$ vs. $MF-IMSA-CG$: Final reconstructions

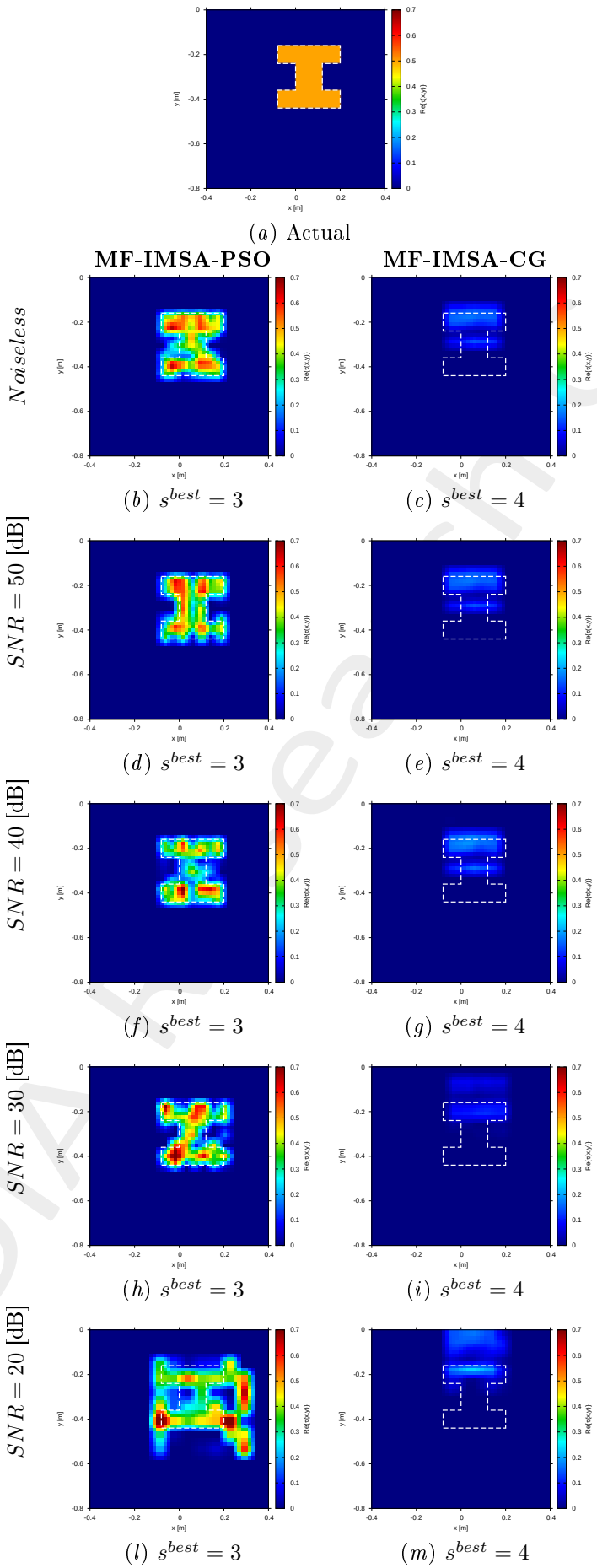

(a) Actual

(b) $s^{best} = 3$ (c) $s^{best} = 4$

(d) $s^{best} = 3$ (e) $s^{best} = 4$

(f) $s^{best} = 3$ (g) $s^{best} = 4$

(h) $s^{best} = 3$ (i) $s^{best} = 4$

(l) $s^{best} = 3$ (m) $s^{best} = 4$

Figure 15: $MF-IMSA-PSO$ vs. $MF-IMSA-CG$: Retrieved dielectric profiles at the $IMSA$ convergence step (s^{best}).

2.2.3 $\varepsilon_{r,obj} = 5.0$ ($\tau = 1.0$) - $MF-IMSA-PSO$ vs. $MF-IMSA-CG$: Final reconstructions

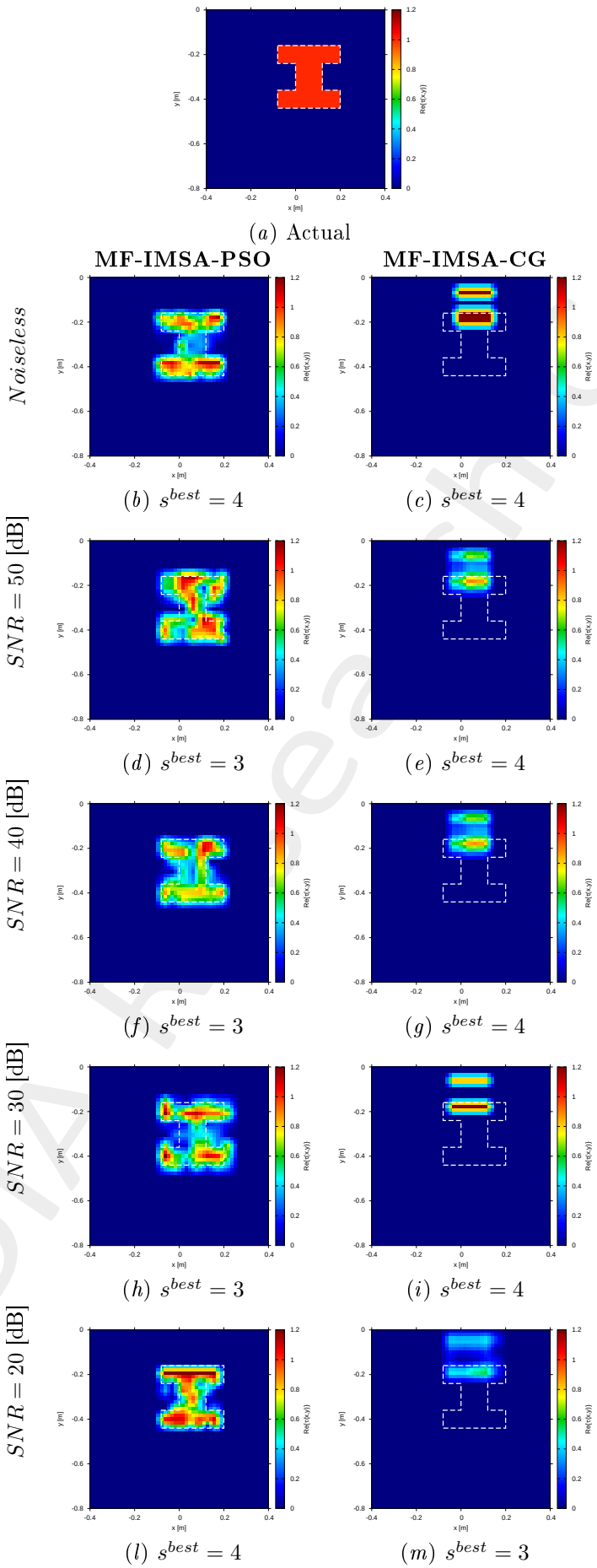

(a) Actual

(b) $s^{best} = 4$ (c) $s^{best} = 4$

(d) $s^{best} = 3$ (e) $s^{best} = 4$

(f) $s^{best} = 3$ (g) $s^{best} = 4$

(h) $s^{best} = 3$ (i) $s^{best} = 4$

(l) $s^{best} = 4$ (m) $s^{best} = 3$

Figure 16: $MF-IMSA-PSO$ vs. $MF-IMSA-CG$: Retrieved dielectric profiles at the $IMSA$ convergence step (s^{best}).

2.2.4 $\varepsilon_{r,obj} = 5.5$ ($\tau = 1.5$) - $MF-IMSA-PSO$ vs. $MF-IMSA-CG$: Final reconstructions

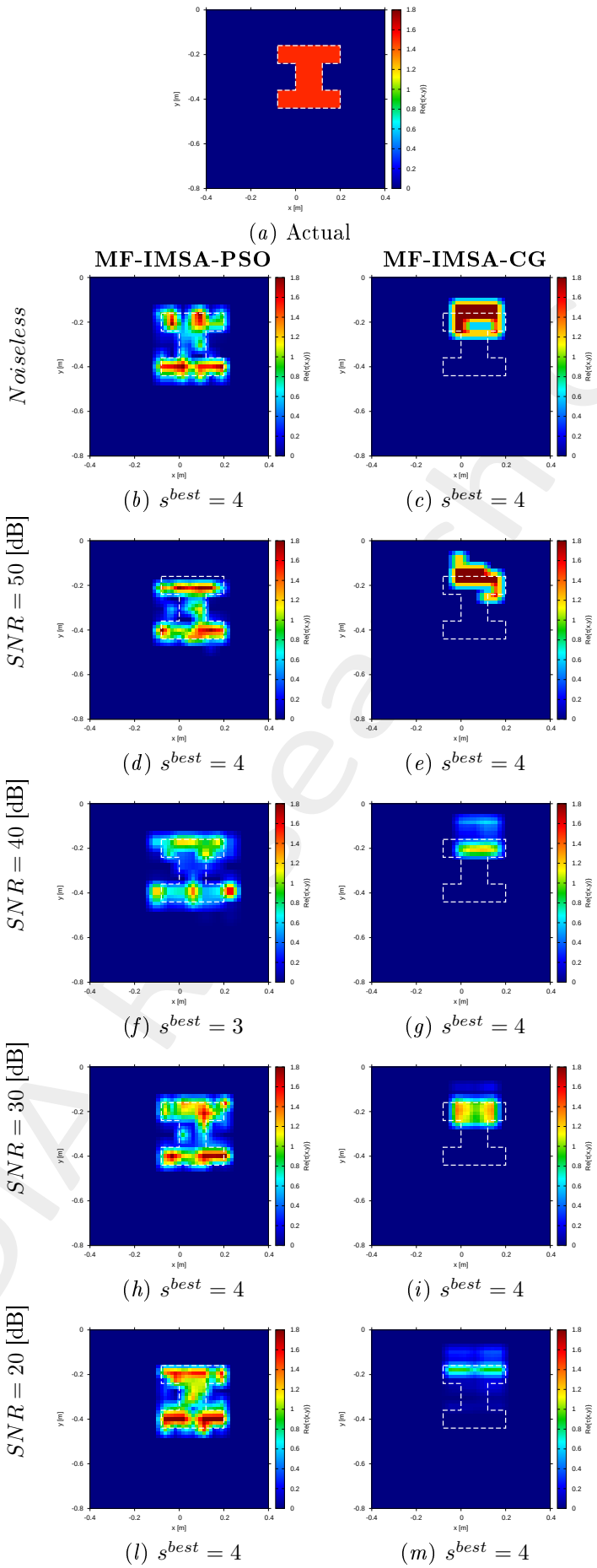

(a) Actual

(b) $s^{best} = 4$ (c) $s^{best} = 4$

(d) $s^{best} = 4$ (e) $s^{best} = 4$

(f) $s^{best} = 3$ (g) $s^{best} = 4$

(h) $s^{best} = 4$ (i) $s^{best} = 4$

(l) $s^{best} = 4$ (m) $s^{best} = 4$

Figure 17: $MF-IMSA-PSO$ vs. $MF-IMSA-CG$: Retrieved dielectric profiles at the $IMSA$ convergence step (s^{best}).

2.2.5 $\varepsilon_{r,obj} = 6.0$ ($\tau = 2.0$) - $MF-IMSA-PSO$ vs. $MF-IMSA-CG$: Final reconstructions

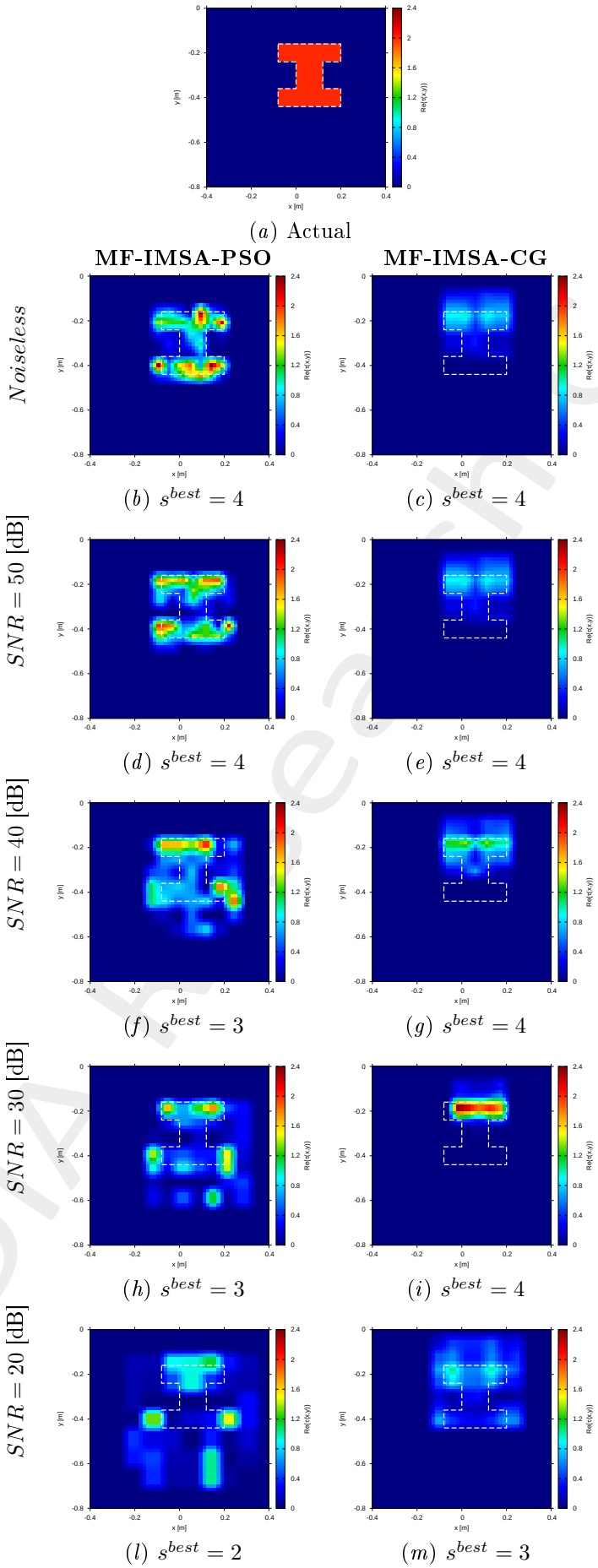

(a) Actual

(b) $s^{best} = 4$ (c) $s^{best} = 4$

(d) $s^{best} = 4$ (e) $s^{best} = 4$

(f) $s^{best} = 3$ (g) $s^{best} = 4$

(h) $s^{best} = 3$ (i) $s^{best} = 4$

(l) $s^{best} = 2$ (m) $s^{best} = 3$

Figure 18: $MF-IMSA-PSO$ vs. $MF-IMSA-CG$: Retrieved dielectric profiles at the $IMSA$ convergence step (s^{best}).

2.2.6 $\varepsilon_{r,obj} = 6.5$ ($\tau = 2.5$) - $MF-IMSA-PSO$ vs. $MF-IMSA-CG$: Final reconstructions

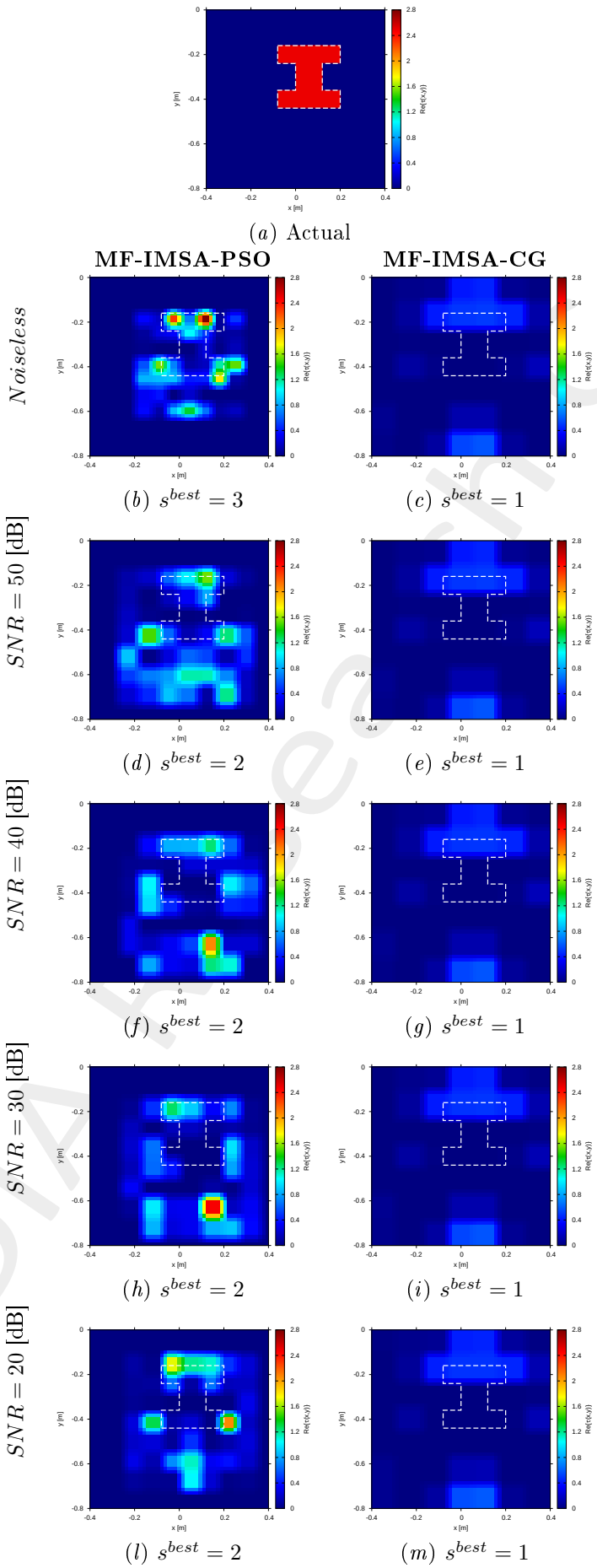

Figure 19: $MF-IMSA-PSO$ vs. $MF-IMSA-CG$: Retrieved dielectric profiles at the $IMSA$ convergence step (s^{best}).

2.2.7 $\varepsilon_{r,obj} = 7.0$ ($\tau = 3.0$) - $MF-IMSA-PSO$ vs. $MF-IMSA-CG$: Final reconstructions

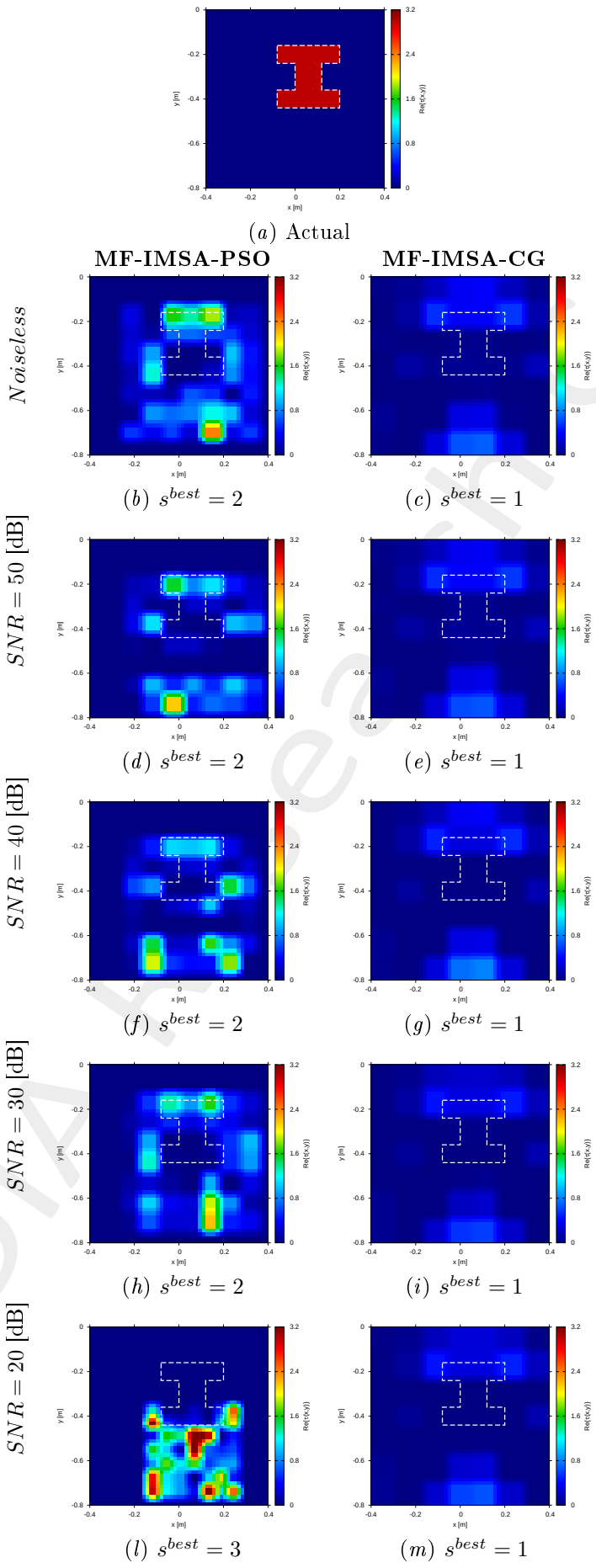

Figure 20: $MF-IMSA-PSO$ vs. $MF-IMSA-CG$: Retrieved dielectric profiles at the $IMSA$ convergence step (s^{best}).

2.2.8 $MF-IMSA-PSO$ vs. $MF-IMSA-CG$: Errors vs. $\varepsilon_{r,obj}$

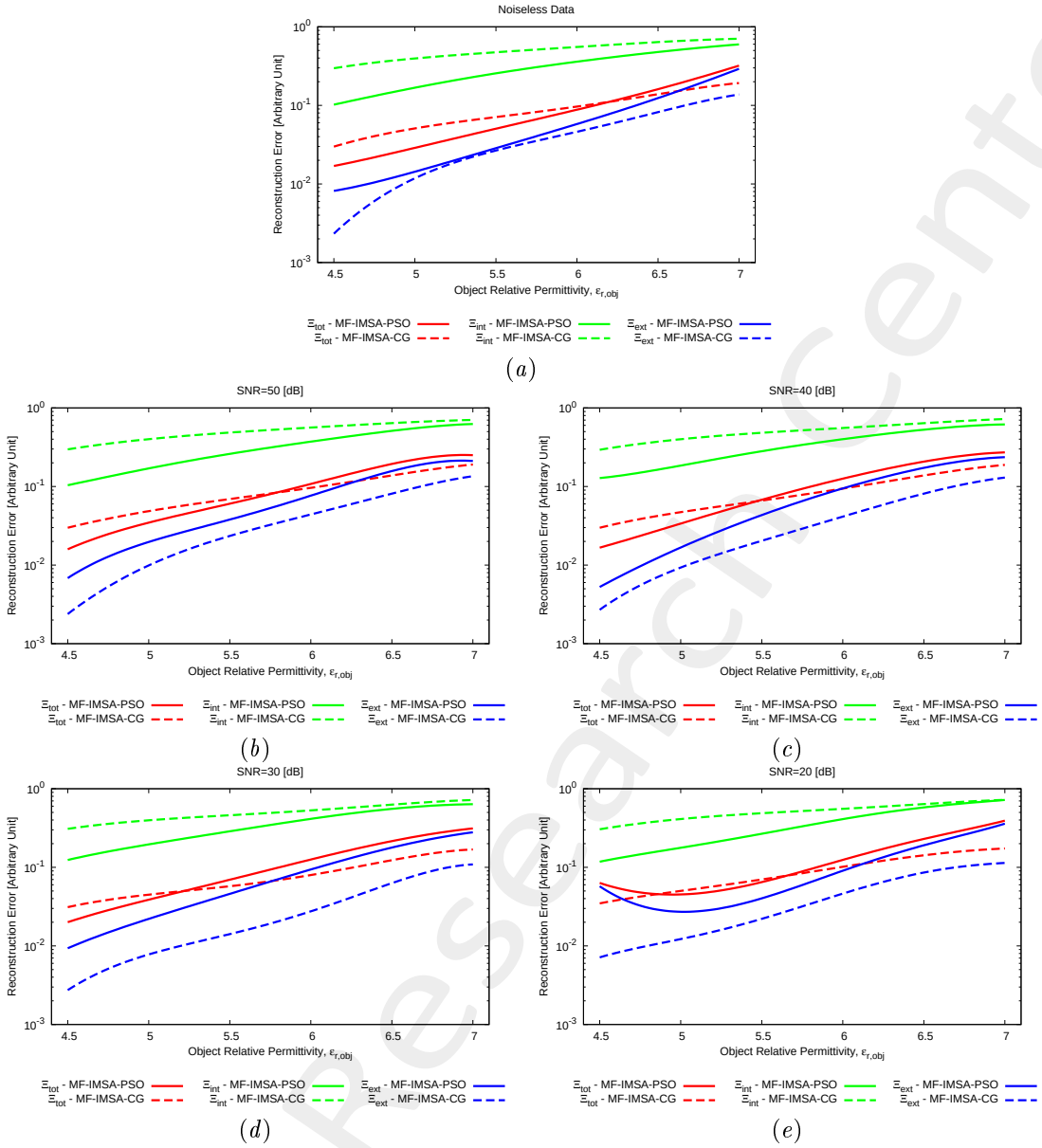

Figure 21: $MF-IMSA-PSO$ vs. $MF-IMSA-CG$: Reconstruction errors vs. the object relative permittivity ($\varepsilon_{r,obj}$).

2.2.9 $MF-IMSA-PSO$ vs. $MF-IMSA-CG$: Errors vs. SNR

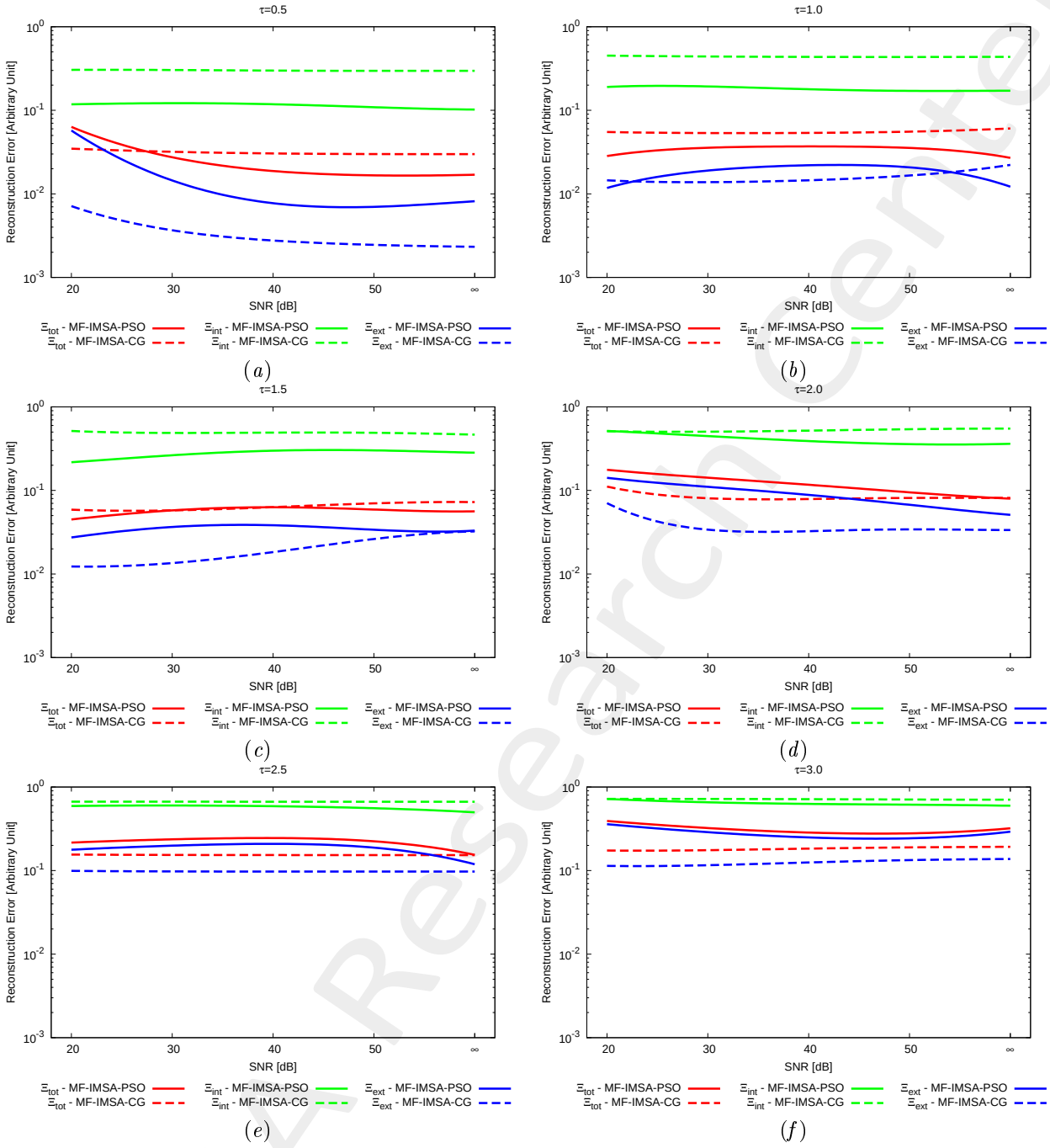

Figure 22: $MF-IMSA-PSO$ vs. $MF-IMSA-CG$: Reconstruction errors vs. SNR.

3 Conclusions

The following main outcomes can be drawn from the reported numerical experiments

- The $MF-IMSA-PSO$ is able to provide a significant performance improvement in terms of achieved solution quality with respect to the $MF-IMSA-CG$;
- The superior accuracy of the $MF-IMSA-PSO$ is given by the exploitation of a stochastic solver (i.e., the PSO), that is more suitable with respect to the CG for minimizing the highly non-linear MF cost function;
- Good reconstructions are yielded by the proposed $MF-IMSA-PSO$ when considering a variation of both the shape and dielectric permittivity of the buried targets.

References

[1] P. Rocca, M. Benedetti, M. Donelli, D. Franceschini, and A. Massa, "Evolutionary optimization as applied to inverse problems," *Inverse Probl.*, vol. 25, pp. 1-41, Dec. 2009.

[2] P. Rocca, G. Oliveri, and A. Massa, "Differential Evolution as applied to electromagnetics," *IEEE Antennas Propag. Mag.*, vol. 53, no. 1, pp. 38-49, Feb. 2011.

[3] M. Salucci, G. Oliveri, and A. Massa, "GPR prospecting through an inverse scattering frequency-hopping multi-focusing approach," *IEEE Trans. Geosci. Remote Sens.*, vol. 53, no. 12, pp. 6573-6592, Dec. 2015.

[4] M. Salucci, L. Poli, and A. Massa, "Advanced multi-frequency GPR data processing for non-linear deterministic imaging," *Signal Processing - Special Issue on 'Advanced Ground-Penetrating Radar Signal-Processing Techniques,'* vol. 132, pp. 306-318, Mar. 2017.

[5] M. Salucci, L. Poli, N. Anselmi and A. Massa, "Multifrequency particle swarm optimization for enhanced multiresolution GPR microwave imaging," *IEEE Trans. Geosci. Remote Sens.*, vol. 55, no. 3, pp. 1305-1317, Mar. 2017.

[6] A. Massa, P. Rocca, and G. Oliveri, "Compressive sensing in electromagnetics - A review," *IEEE Antennas Propag. Mag.*, pp. 224-238, vol. 57, no. 1, Feb. 2015.

[7] A. Massa and F. Texeira, Guest-Editorial: Special Cluster on Compressive Sensing as Applied to Electromagnetics, *IEEE Antennas Wireless Propag. Lett.*, vol. 14, pp. 1022-1026, 2015.

[8] N. Anselmi, G. Oliveri, M. Salucci, and A. Massa, "Wavelet-based compressive imaging of sparse targets," *IEEE Trans. Antennas Propag.*, vol. 63, no. 11, pp. 4889-4900, Nov. 2015.

[9] G. Oliveri, N. Anselmi, and A. Massa, "Compressive sensing imaging of non-sparse 2D scatterers by a total-variation approach within the Born approximation," *IEEE Trans. Antennas Propag.*, vol. 62, no. 10, pp. 5157-5170, Oct. 2014.

[10] T. Moriyama, G. Oliveri, M. Salucci, and T. Takenaka, "A multi-scaling forward-backward time-stepping method for microwave imaging," *IEICE Electron. Expr.*, vol. 11, no. 16, pp. 1-12, Aug. 2014.

[11] T. Moriyama, M. Salucci, M. Tanaka, and T. Takenaka, "Image reconstruction from total electric field data with no information on the incident field," *J. Electromagnet. Wave.*, vol. 30, no. 9, pp. 1162-1170, 2016.

[12] F. Viani, L. Poli, G. Oliveri, F. Robol, and A. Massa, "Sparse scatterers imaging through approximated multi-task compressive sensing strategies," *Microw. Opt. Technol. Lett.*, vol. 55, no. 7, pp. 1553-1557, Jul. 2013.

[13] M. Salucci, N. Anselmi, G. Oliveri, P. Calmon, R. Miorelli, C. Reboud, and A. Massa, "Real-time NDT-NDE through an innovative adaptive partial least squares SVR inversion approach," *IEEE Trans. Geosci. Remote Sens.*, vol. 54, no. 11, pp. 6818-6832, Nov. 2016.

[14] L. Poli, G. Oliveri, and A. Massa, "Imaging sparse metallic cylinders through a local shape function bayesian compressing sensing approach," *J. Opt. Soc. Am. A*, vol. 30, no. 6, pp. 1261-1272, Jun. 2013.

[15] M. Donelli, D. Franceschini, P. Rocca, and A. Massa, "Three-dimensional microwave imaging problems solved through an efficient multiscaling particle swarm optimization," *IEEE Trans. Geosci. Remote Sensing*, vol. 47, no. 5, pp. 1467-1481, May 2009.